Journal of Solid State Chemistry 183 (2010) 2190–2195

Contents lists available at ScienceDirect

Journal of Solid State Chemistry

journal homepage: www.elsevier.com/locate/jssc

New perovskite-based manganite $Pb_2Mn_2O_5$

Joke Hadermann [a,*], Artem M. Abakumov [a,c], Tyché Perkisas [a], Hans D'Hondt [a], Haiyan Tan [a], Johan Verbeeck [a], Vladimir P. Filonenko [b], Evgeny V. Antipov [c], Gustaaf Van Tendeloo [a]

[a] Department of Physics, EMAT, University of Antwerp, Groenenborgerlaan 171, B-2020 Antwerp, Belgium
[b] Vereshchagin Institute of High-Pressure Physics, Russian Academy of Sciences, Troitsk, Moscow Oblast 142092, Russia
[c] Department of Chemistry, Moscow State University, 119991 Moscow, Russia

ARTICLE INFO

Article history:
Received 26 May 2010
Received in revised form
16 July 2010
Accepted 18 July 2010
Available online 24 July 2010

Keywords:
Manganite
TEM
Lone pair
Perovskite
Crystallographic shear plane

ABSTRACT

A new perovskite based compound $Pb_2Mn_2O_5$ has been synthesized using a high pressure high temperature technique. The structure model of $Pb_2Mn_2O_5$ is proposed based on electron diffraction, high angle annular dark field scanning transmission electron microscopy and high resolution transmission electron microscopy. The compound crystallizes in an orthorhombic unit cell with parameters $a=5.736(1)$ Å $\approx \sqrt{2}a_p$, $b=3.800(1)$ Å $\approx a_p$, $c=21.562(6)$ Å $\approx 4\sqrt{2}a_p$ (a_p—the parameter of the perovskite subcell) and space group *Pnma*. The $Pb_2Mn_2O_5$ structure consists of quasi two-dimensional perovskite blocks separated by $1/2[110]_p(\bar{1}01)_p$ crystallographic shear planes. The blocks are connected to each other by chains of edge-sharing MnO_5 distorted tetragonal pyramids. The chains of MnO_5 pyramids and the MnO_6 octahedra of the perovskite blocks delimit six-sided tunnels accommodating double chains of Pb atoms. The tunnels and pyramidal chains adopt two mirror-related configurations ("left" L and "right" R) and layers consisting of chains and tunnels of the same configuration alternate in the structure according to an -L–R–L–R-sequence. The sequence is sometimes locally violated by the appearance of -L–L- or -R–R-fragments. A scheme is proposed with a Jahn–Teller distortion of the MnO_6 octahedra with two long and two short bonds lying in the *a*–*c* plane, along two perpendicular orientations within this plane, forming a *d*-type pattern.

1. Introduction

Perovskite based lead manganites have never been observed with ambient pressure synthesis, whereas the application of a high pressure high temperature technique resulted in several complex oxides with a perovskite-type structure in the Pb–Mn–O system. $PbMnO_3$ synthesized under high pressure has the 6H hexagonal perovskite structure [1] and transforms into a tetragonally distorted 3C $PbMnO_{3-\delta}$ perovskite at 15 GPa [2]. Another phase formed under high pressure is $Pb_{13}Mn_9O_{25}$ [3] with a tetragonal oxygen- and manganese-deficient perovskite-based structure, in which MnO_6 octahedra and MnO_5 tetragonal pyramids form a network by sharing common corners. Tunnels are formed in that network because of an ordered arrangement of vacancies at the *B* sublattice. Under high pressure also the anion deficient compound $Pb_{0.9}MnO_{2.63}$ with continuous quasi-2D perovskite blocks separated by planar interfaces is formed [4]. A displacement of the blocks with respect to each other over $1/2[110]_p$ occurs at the interfaces, which thus acquire crystallographic properties similar to those of the crystallographic shear (CS) planes in binary transition metal oxides. The concept of crystallographic shear planes in perovskites was elaborated in detail based on transmission electron microscopy investigations of Fe-containing perovskites [5–7]. Different orientations of the $1/2[110](h0l)_p$ CS planes with respect to the perovskite subcell and a different thickness of the perovskite module between two consecutive CS planes, give rise to a homologous series $(Pb,A)_{4p+3q}B_{4(p+q)}O_{10p+9q}$ (A=Pb, Ba, Sr, B=Fe, Mn), where p and q are related to the $(h0l)$ indices of the CS planes [8–11]. The shear operation changes the connectivity scheme of the metal-oxygen polyhedra, replacing corner-sharing BO_6 octahedra by edge-sharing BO_5 distorted tetragonal pyramids (Fig. 1). Chains of these pyramids, connected to the BO_6 octahedra of the perovskite modules, delimit six-sided tunnels occupied by two columns of Pb atoms, providing sufficient space for the localization of their lone electron pairs.

The simplest variant of a CS structure is realized in $Pb_{2-x}Ba_xFe_2O_5$ ($x=0.6$–1.0) [12] (Fig. 2a) and $Pb_{4/3}Sr_{2/3}Fe_2O_5$ [13] (Fig. 2b), where only $1/2[110]_p(\bar{1}01)_p$ interfaces as are present (Fig. 1). In these structures, the chains of edge-sharing FeO_5 pyramids occur in two mirror-related configurations ("left" L and "right" R). The correspondence of a chain configuration to either the label L or otherwise R is arbitrary. The tunnels delimited by L or R chains will be called L or R tunnels, respectively. At room temperature, the L and R chains are fully ordered into alternating layers. A phase transition between an ordered and

* Corresponding author. Fax: +32 3265 3257.
E-mail address: joke.hadermann@ua.ac.be (J. Hadermann).

0022-4596/$ - see front matter © 2010 Elsevier Inc. All rights reserved.
doi:10.1016/j.jssc.2010.07.032

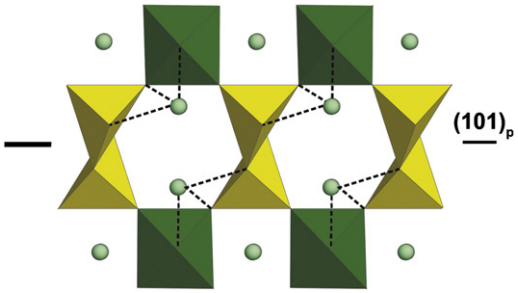

Fig. 1. Scheme of a $1/2[110](\bar{1}01)_p$ CS plane in perovskites. The distorted BO_5 tetragonal pyramids are yellow (light in grayscale), the BO_6 octahedra are green (dark in grayscale) and the Pb atoms are light green (for interpretation of the references to color in this figure legend, the reader is referred to the web version of this article).

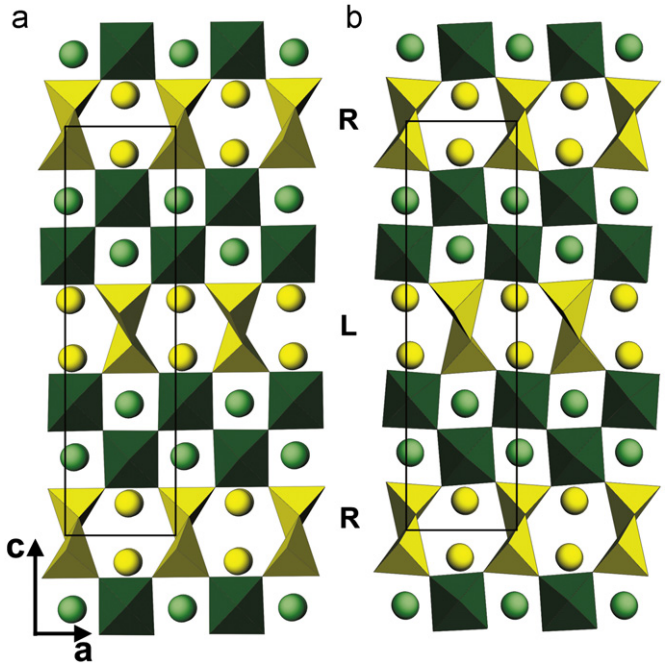

Fig. 2. Structure of (a) $Pb_{2-x}Ba_xFe_2O_5$ ($x=0.6$–1.0) [12] and (b) $Pb_{4/3}Sr_{2/3}Fe_2O_5$ [13]. FeO_5 tetragonal pyramids are yellow (light in grayscale), FeO_6 octahedra are green (dark in grayscale), Pb atoms in the six-sided tunnels are yellow and the Pb/Sr/Ba atoms belonging to the perovskite modules are green (for interpretation of the references to color in this figure legend, the reader is referred to the web version of this article).

disordered arrangement of the chains was detected in $PbBaFe_2O_5$ around 270°C. In $Pb_{4/3}Sr_{2/3}Fe_2O_5$ the perovskite block is subjected to a noticeable tilting distortion. This is not the case in $PbBaFe_2O_5$, in agreement with the larger size of the Ba^{2+} cations, occupying the A-positions in the perovskite blocks.

In this paper, we report the synthesis and structure determination of the Mn-based $1/2[110]_p(\bar{1}01)_p$ CS structure $Pb_2Mn_2O_5$. Although the structure is similar to that of $Pb_{4/3}Sr_{2/3}Fe_2O_5$ and $PbBaFe_2O_5$, there is experimental evidence for a Jahn–Teller distortion of the MnO_6 octahedra in $Pb_2Mn_2O_5$, which is compatible with the observed defect structure in this material.

2. Experimental

A mixture of PbO and Mn_2O_3 (Reakhim, "pure for analysis" purity grade) with bulk composition $Pb_2Mn_2O_5$ was used as a starting material. This powder was pressed into pellets of 3 mm in height and 5 mm in diameter. The pellets were placed in gold capsules to avoid a chemical reaction between the specimen and the surrounding material. The thermobaric synthesis was carried out using high pressure chambers of the toroid-type, consisting of two hard metal anvils with a special profile [14]. The pressure was generated in a lithographic limestone cell placed between the anvils. The pressure values were calibrated at room temperature by measuring the electrical conductivity and fixing the phase transition of Bi I–II (2.55 GPa) and Bi IV–V(7.7 GPa). The temperature was measured by chromel–alumel thermocouples. The high-pressure treatment was carried out under the following experimental conditions: pressure of ~7.0 GPa, temperature range of 800–1000 °C. After stabilization of the applied pressure, the samples were heated up to the desired temperature and held at that temperature for 5 min. Then, the samples were quenched to room temperature before the pressure was released.

The X-ray powder diffraction (XRPD) pattern was collected on a Huber G670 Guinier diffractometer (Cu$K\alpha$1 radiation, curved Ge monochromator, transmission mode and image plate).

The samples for transmission electron microscopy (TEM) were prepared by crushing the powder sample in ethanol and depositing the grains on a holey carbon grid. Selected area precession electron diffraction (PED) patterns were recorded using a Philips CM20 microscope, equipped with a "Spinning Star" precession instrument. The *in situ* heating selected area electron diffraction experiment was performed with a GATAN heating holder on the Philips CM20 microscope. High resolution electron microscopy (HRTEM) images were recorded on a JEOL 4000EX microscope. Energy dispersive X-ray (EDX) spectra were obtained on the Philips CM20 with an Oxford INCA system. The HRTEM images were simulated using the MacTempas software. High angle annular dark field scanning transmission electron microscopy (HAADF-STEM) images were recorded on a Tecnai G2 microscope. Calculated HAADF-STEM images were obtained using the QSTEM software [15].

3. Results

3.1. Unit cell, space symmetry and chemical composition.

The multiphase "$Pb_2Mn_2O_5$" sample was investigated using TEM; it showed two major coexisting phases, both perovskite based. A structure solution using X-ray powder diffraction data was not possible, due to an overlap of the strong reflections and the presence of unidentified admixtures. Therefore, the structures were solved using TEM. Only one of the phases will be discussed in the current paper. The structure solution of the other phase, which has a composition $Pb_{13}Mn_9O_{25}$ and a considerably different structure (as described in the introduction), has been published separately [3].

A tilt series over different zones of the phase under consideration was obtained. The PED patterns of the main zones are shown in Fig. 3. All PED patterns could be indexed using the approximate cell parameters $a \approx 5.8$ Å $\approx \sqrt{2}a_p$, $b \approx 3.8$ Å $\approx a_p$, $c \approx 21.6$ Å $\approx 4\sqrt{2}a_p$ (a_p=the parameter of the perovskite sublattice) and show reflection conditions $h\,k\,l$: no conditions, $0\,k\,l$: $k+l=2n$, $h\,0\,l$: no conditions, $h\,k\,0$: $h=2n$. This corresponds to the extinction symbol $Pn-a$ and leaves as possible space groups $Pn2_1a$ and $Pnma$. The most symmetric, $Pnma$, will be used. An attempt to select the reflections belonging to the target phase on the XRPD pattern and index them with the unit cell determined from the PED data resulted in the lattice parameters $a=5.736(1)$Å, $b=3.800(1)$Å and $c=21.562(6)$Å.

The cation composition of the phase was determined by EDX analysis on 20 crystallites and shows a composition

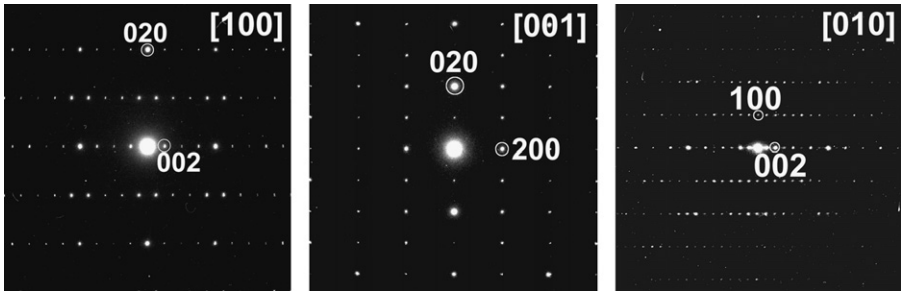

Fig. 3. PED patterns of the main zones of $Pb_2Mn_2O_5$.

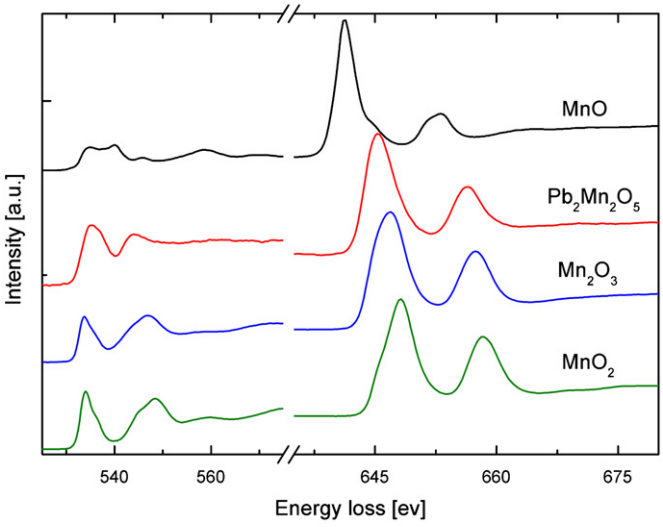

Fig. 4. The O K edge and Mn L edge of $Pb_2Mn_2O_5$ after power law background subtraction, compared to the Mn L edge of standards with V(Mn)=+2 (MnO), +3 (Mn_2O_3) and +4 (MnO_2).

$Pb_{0.98(6)}Mn_{1.02(6)}O_x$. To determine the oxygen content, the manganese valence (V_{Mn}) was obtained from EELS measurements. The distance of the energy onset between the oxygen K edge and the Mn $L_{2,3}$ edge was measured and compared to a linear curve obtained from measuring standards [16], using the correction for nonlinear dispersion in the spectrometer suggested in [3]; this gives as the linear relation between this energy onset difference (ΔE) and the Mn valence (V_{Mn}): $\Delta E = a + bV_{Mn}$ with $a = 103.02 \pm 0.18$ eV and $b = 2.26 \pm 0.06$ eV/Valence. From the analysis of 30 repeating spectra on a crystal, it was found that the edge onset difference of oxygen K and manganese $L_{2,3}$ edges for $Pb_{0.98(6)}Mn_{1.02(6)}O_x$ is 109.93(18) eV (Fig. 4). From the relation above, the Mn valence can then be estimated as $V_{Mn} = +3.05(16)$. The oxygen content calculated from the EDX and EELS results, assuming Pb^{2+}, is then equal to 2.53(14). The composition derived from EDX and EELS results is, therefore, $Pb_{0.98(6)}Mn_{1.02(6)}O_{2.53(14)}$ or $Pb_2Mn_2O_5$.

3.2. HAADF-STEM and HRTEM observations

HAADF-STEM images along [010] are shown in Figs. 5 and 6. On these images the intensity of the bright dots is related to the average atomic number of the atomic column as $\sim Z^n$ ($1.5 < n < 2$). Therefore the brighter dots correspond to the Pb atom columns, the weaker ones to the Mn–O columns. Pure oxygen columns are too weak to be detected on these images. The cation positions, revealed from the HAADF-STEM images are very similar to those in the $PbBaFe_2O_5$ [12] and $Pb_{4/3}Sr_{2/3}Fe_2O_5$ [13]

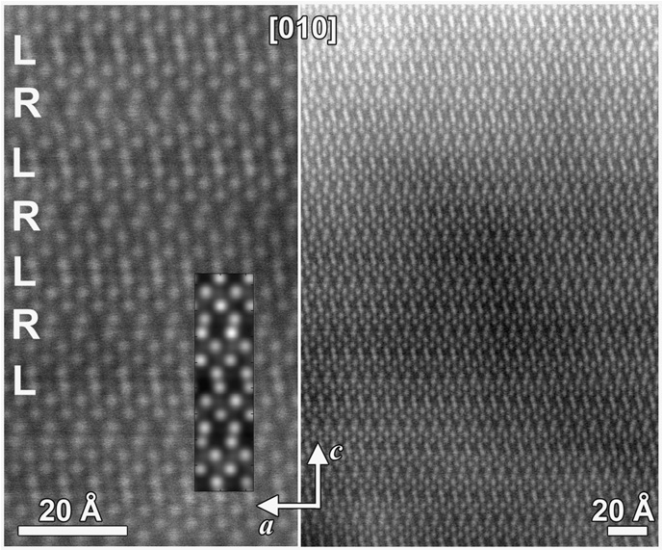

Fig. 5. HAADF-STEM images of $Pb_2Mn_2O_5$ along [010] in close-up (left) and overview (right). For the close-up, layers with left (L) and right (R) configurations are indicated; a calculated HAADF-STEM using the model of Fig. 9 and Table 1 is inserted.

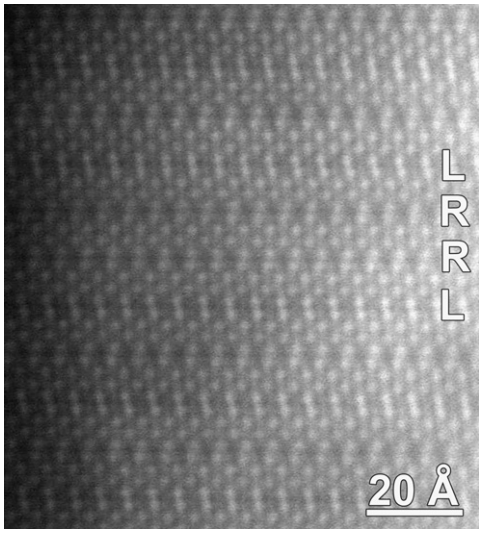

Fig. 6. HAADF-STEM image along [010] of an area showing defects in the L–R–L–R sequence of the layers.

structures with $1/2[110]_p(\bar{1}01)_p$ CS planes: the dots corresponding to the projections of the Pb columns in the six-sided tunnels form pairs arranged into horizontal layers tracing the $1/2[110]_p(\bar{1}01)_p$

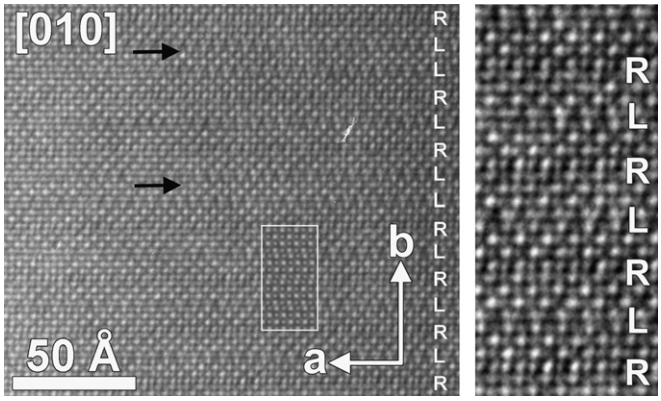

Fig. 7. HRTEM image of $Pb_2Mn_2O_5$ along [010], at the left an overview image, at the right an enlarged part of that image. Antiphase boundaries are indicated by black arrows.

CS planes. Taking into account the same $A_2B_2O_5$ chemical composition and the same *Pnma* space group for $Pb_2Mn_2O_5$, $PbBaFe_2O_5$ and $Pb_{4/3}Sr_{2/3}Fe_2O_5$, one can suggest that these compounds are isostructural. The pairs of Pb columns occur in two clearly distinct configurations, being tilted left (L) and right (R) around the *b*-axis, which results in a sideways shift of the Pb columns from the *c*-axis. These two configurations are related to the presence of L and R tunnels. In agreement with the *Pnma* space symmetry, layers of L tunnels and layers of R tunnels alternate along the *c*-axis in an -L–R–L–R-sequence. The right-hand side of Fig. 5 shows a larger area, exhibiting perfect order between alternating layers of L and R tunnels. However, in some crystallites a violation is observed of this ordered alternation by the occurrence of two successive L or R layers (Fig. 6).

High resolution transmission electron microscopy (HRTEM) images along different zone axes were obtained in order to confirm the structure model. A representative HRTEM image along [010] is shown in Fig. 7. At this defocus value and thickness, all bright dots represent columns of cations and the relation of the HRTEM image to the structure and to the HAADF-STEM image is clear. The bigger and brighter dots are the Pb columns, the less bright ones, in the perovskite block as well as at the CS plane, are the projections of the Mn–O columns. Again, the L and R tunnels can be distinguished by a tilt of the Pb pairs located at the CS plane. The L and R layer sequence in the HRTEM image shows a perfect alternation at the bottom, while higher up twice an extra L layer occurs. Such defects can be interpreted as antiphase boundaries (APB), which are confined to the (001) plane and separate two parts of the structure displaced with respect to each other by 1/2[111], as clarified on the structural model of Fig. 8.

The material was heated *in situ* in the TEM to examine if a phase transition between ordered and disordered arrangement of the L and R layers occurs, such as observed around ~540 K for $PbBaFe_2O_5$ [12]. No phase transition was observed during heating up to 770 K, at which temperature the compound decomposes.

4. Discussion

The structure of $Pb_2Mn_2O_5$ is similar to the low-temperature form of $PbBaFe_2O_5$ [12] and to $Pb_{4/3}Sr_{2/3}Fe_2O_5$ [13]. The structure is built up from perovskite blocks separated by periodic $1/2[110]_p(\bar{1}01)_p$ CS planes. At the CS planes the MnO_5 tetragonal pyramids are grouped into chains by edge-sharing. The chains can adopt two mirror-related configurations, termed L and R. On the HAADF-STEM images the configuration of the tetragonal pyramidal chains themselves is not directly visible, but the configuration

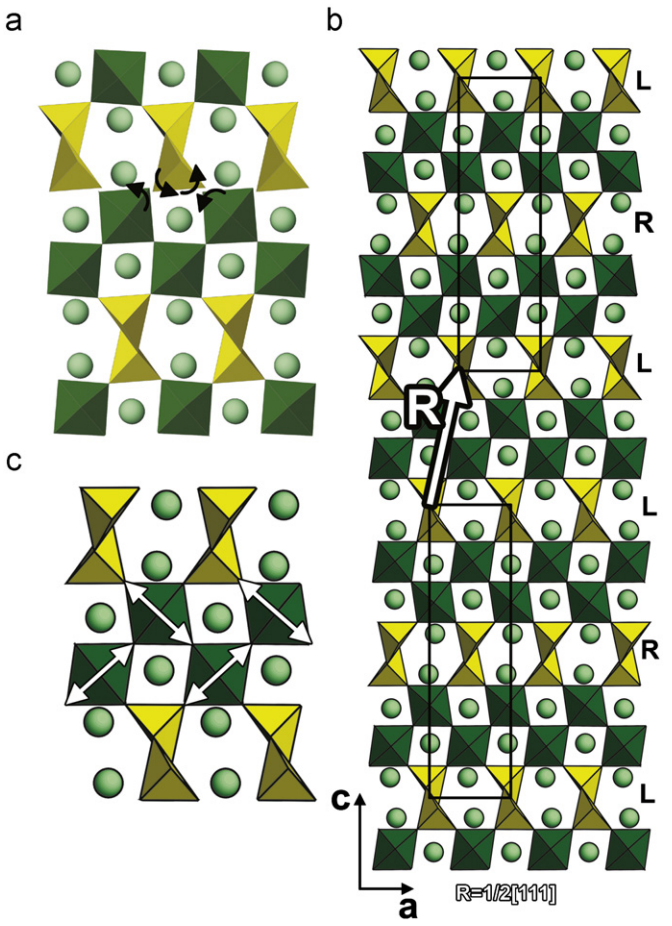

Fig. 8. (a) Scheme showing the incompatibility of tilted isotropic octahedra with antiphase boundaries. The black arrows indicate the rotation directions of the corners. (b) Model for the antiphase boundaries in $Pb_2Mn_2O_5$. The black rectangles outline the unit cell, the displacement vector introduced by the antiphase boundary is indicated by the white R-vector. (c) Scheme showing the alternation of the long Mn–O bonds within the plane. The double-sided arrows are superimposed over the long bonds.

of the CS planes can be judged from the positions of the Pb columns in the six-sided tunnels. According to the HAADF-STEM and TEM images, chains of different configurations are arranged into separate layers and never occur together in one layer. Thus, we can distinguish between L- and R-type CS planes, according to the configuration of the chains and the six-sided tunnels between them in which the Pb atoms reside.

The configuration in neighboring CS planes is coupled through the tilting distortions of the interleaving perovskite blocks. According to the *Pnma* space symmetry, the perovskite block can undergo a cooperative octahedral tilting distortion with the only symmetry allowed rotation component being around the *b*-axis ($a^0b^+a^0$ in Glazer's notation). Since the corner-sharing of the BO_6 octahedra and BO_5 tetragonal pyramids must be preserved, the cooperative octahedral distortion enforces the tetragonal pyramidal chains to adopt either an R or an L configuration. The rotation directions of both sides of the perovskite block are opposite, due to an even number of BO_6 octahedra in the perovskite block between two consecutive CS planes. This causes the R and L CS planes to alternate along the *c*-axis. This scenario is realized in the $Pb_{4/3}Sr_{2/3}Fe_2O_5$ structure, where the FeO_6 octahedra are rotated by ~4° about the *b*-axis. In $PbBaFe_2O_5$ the octahedral rotation is suppressed, and this weakens the link between neighboring CS planes. Indeed, above

~540 K the *Pnma* $PbBaFe_2O_5$ structure with ordered L and R CS planes transforms into the *Imma* structure where the R and L configurations are disordered along the *c*-axis. [12]

It can be assumed that the sideways displacement of the Pb columns from the *c*-axis correlates with the magnitude of octahedral rotation. This can be seen from the comparison of the models and calculated HAADF-STEM images shown in Fig. 9 of $PbBaFe_2O_5$ (Pb columns in tunnels above each other along *c*) and $Pb_{4/3}Sr_{2/3}Fe_2O_5$ (Pb columns not directly above each other along *c*). From the experimental HAADF-STEM and HRTEM images of $Pb_2Mn_2O_5$ (Figs. 5–7), it is clear that in $Pb_2Mn_2O_5$ the Pb columns are noticeably shifted from the *c*-axis. Therefore, it is plausible that in $Pb_2Mn_2O_5$ the octahedral rotations in the perovskite block occur with a rotation angle not smaller than that in $Pb_{4/3}Sr_{2/3}Fe_2O_5$. However, the APBs experimentally observed in $Pb_2Mn_2O_5$ are not compatible with the $a^0b^+a^0$ rotation pattern of quasi-isotropic MnO_6 octahedra as present in $Pb_{4/3}Sr_{2/3}Fe_2O_5$. This is most easily visually clarified by schematically introducing such APB into the structure of $Pb_{4/3}Sr_{2/3}Fe_2O_5$ (Fig. 8a). The corner-sharing connectivity between the MnO_6 octahedra and MnO_5 tetragonal pyramids is lost at the APB and can be restored only at the cost of a deformation of the coordination polyhedra for the Mn cations.

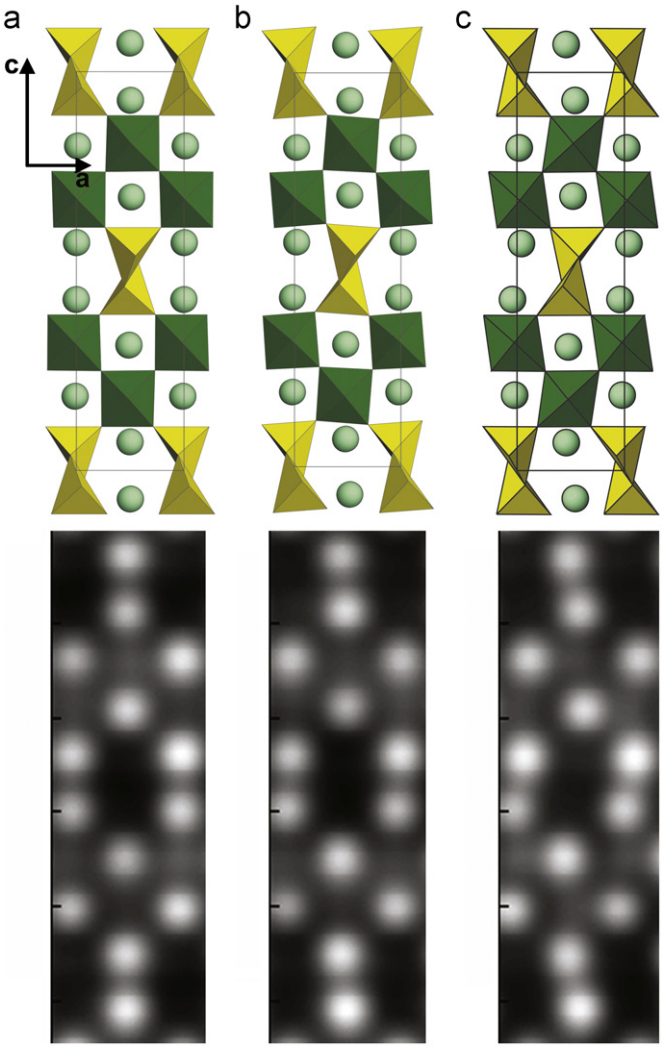

Fig. 9. Structures and calculated HAADF-STEM images for (a) $PbBaFe_2O_5$, (b) $Pb_{4/3}Sr_{2/3}Fe_2O_5$ and (c) $Pb_2Mn_2O_5$. The positions of the Pb columns are shown as green spheres, Mn and oxygen form MnO_6 octahedra (green/dark in grayscale) and MnO_5 distorted tetragonal pyramids (yellow/light in grayscale). Models and calculated images are on the same scale (for interpretation of the references to color in this figure legend, the reader is referred to the web version of this article).

One possibility is that the required deformation is provided by a Jahn–Teller distortion of the MnO_6 octahedra. The Jahn–Teller effect is intrinsic in Mn^{3+} cations in an octahedral oxygen environment. The two most common modes of the Jahn–Teller distortion of BO_6 octahedra are the Q_2 mode, where two B–O bonds lengthen and two bonds contract, and the Q_3 mode with two elongated and four contracted B–O bonds [17,18]. In $Pb_2Mn_2O_5$ an elongation of the Mn–O bond along the *b*-axis can be excluded since the Mn–O distance in this direction is only ~1.90 Å (as estimated from the unit cell *b*-parameter). Being compared with the Mn–O interatomic distances in orthorhombic $LaMnO_3$ (2×2.18, 2×1.97 and 2×1.91 Å) [19], this corresponds to the contracted bond length. We therefore assume that the MnO_6 octahedra are Jahn–Teller distorted, with two long Mn–O bonds and two short (or intermediate) Mn–O bonds lying in the *a*–*c* plane. The longer and shorter bonds in two neighboring MnO_6 octahedra are aligned along two mutually perpendicular directions (Fig. 8c). The ordering pattern of the Mn–O bonds does not alter along the *b*-axis. A similar ordering pattern of Jahn–Teller distorted octahedra is also found in the perovskite $KCuF_3$ [20,21], where different configurations are denoted according to whether the orientation of the long bonds rotates over 90° in the same plane from layer to layer (types *a* and *b*, respectively, without and with stacking disorder), or whether all layers have the same orientation of the long bonds (types *c* and *d*, respectively, with and without stacking disorder). The order in $Pb_2Mn_2O_5$ corresponds to the type "*d*", since the orientation of the long bonds alternates in the *a*–*c* plane, but is the same for consecutive layers along the *b*-axis.

The combination of the octahedral rotation with the Jahn–Teller deformation helps to relieve the strain at the APB. The ordered pattern of the long and short Mn, respectively, O bonds switches to its mirror-reflected configuration at the APB (Fig. 8b) thus restoring the corner-sharing connectivity between the MnO_6 and MnO_5 polyhedra. The approximate atomic coordinates for the model shown in Fig. 8b and c are provided in Table 1. The atomic coordinates for the Pb atoms were directly measured from the HAADF-STEM images using the software CRISP. For this, first the average image was calculated over an area of approximately 300 Å in diameter, using the projected symmetry *p2gg* for [010], as determined by the extinction symbol $Pn-a$ obtained from the PED patterns. From this average image the *x*–*z* coordinates can be directly measured, while the *y* coordinate is the same as in the similar structures $PbBaFe_2O_5$ and $Pb_{4/3}Sr_{2/3}Fe_2O_5$. The proposed model was verified by calculating HAADF-STEM and TEM images. A calculated HAADF-STEM image for $Pb_2Mn_2O_5$ is shown in Fig. 9c. For easy comparison, the [010] projection of the structures of $PbBaFe_2O_5$ and $Pb_{4/3}Sr_{2/3}Fe_2O_5$ and their calculated

Table 1
Atomic coordinates for $Pb_2Mn_2O_5$ (S.G. *Pnma*, $a=5.736(1)$ Å, $b=3.800(1)$ Å, $c=21.562(6)$ Å).

Atom	*x/a*	*y/b*	*z/c*
Pb1	0.9495	1/4	0.4337
Pb2	0.9157	1/4	0.1853
Mn1	0.4683	1/4	0.4451
Mn2	0.9700	1/4	0.3200
O1	0.9746	3/4	0.3216
O2	0.7628	1/4	0.2507
O3	0.1853	1/4	0.3895
O4	0.6903	1/4	0.3901
O5	0.4240	3/4	0.4637

HAADF-STEM images are shown in Figs. 9a and b, respectively. A calculated [010] HAADF-STEM image for a thickness of 40 Å is shown for each structure, on the same scale as the structure model shown above the simulation. The difference between the $PbBaFe_2O_5$, $Pb_{4/3}Sr_{2/3}Fe_2O_5$ and $Pb_2Mn_2O_5$ structures becomes clear from comparing the positions of the projections of the Pb columns in the six-sided tunnels. An extended version of the calculated image is also inserted in Fig. 5, and matches well with the experimental image. Using the same model, a calculated HRTEM image is inserted into Fig. 7, calculated at a focus value of $f=-700$ Å and a thickness $t=28$ Å, also showing an excellent agreement between the simulated and experimental images.

$Pb_2Mn_2O_5$ belongs to the family of perovskite-based compounds with general composition $(Pb,A)_{4p+3q}B_{4(p+q)}O_{10p+9q}$ and with different $1/2[110]_p(h0l)_p$ crystallographic shear structures [5–11], with in this case $p=1$ and $q=0$, thus representing the simplest member of this family. These findings allow envisaging the existence of other perovskites with different p and q in the Pb–Mn–O system, which could be prepared using the high pressure high temperature technique. This investigation is now underway.

Acknowledgments

This work was supported by the Research Foundation—Flanders (FWO G.0184.09N and 1.5.005.08) and BOF—University of Antwerp (23047). The authors acknowledge financial support from the European Union under the Framework 6 program under a contract for an Integrated Infrastructure Initiative. Reference 026019 ESTEEM. Haiyan Tan acknowledges the financial support from FWO-Vlaanderen (Project no. G.0147.06).

References

[1] C. Bougerol, M.F. Gorius, P. Bordet, I.E. Grey, Acta Crystallogr. A 58 (Suppl.) (2002) C23.
[2] K. Oka, M. Azuma, S. Hirai, A.A. Belik, H. Kojitani, M. Akaogi, M. Takano, Y. Shimakawa, Inorg. Chem. 48 (2009) 2285–2288.
[3] J. Hadermann, A.M. Abakumov, A.A. Tsirlin, V.P. Filonenko, J. Gonnissen, H. Tan, J. Verbeeck, M. Gemmi, E.V. Antipov, H. Rosner, Ultramicroscopy 110 (2010) 881.
[4] C. Bougerol, M.F. Gorius, I.E. Grey, J. Solid State Chem. 169 (2002) 131.
[5] A.M. Abakumov, J. Hadermann, G. Van Tendeloo, E.V. Antipov, J. Am. Ceram. Soc. 91 (6) (2008) 1807.
[6] G. Van Tendeloo, J. Hadermann, A.M. Abakumov, E.V. Antipov, J. Mater. Chem. 19 (18) (2009) 2660.
[7] E.V. Antipov, A.M. Abakumov, S.Ya. Istomin, Inorg. Chem. 47 (2008) 8543.
[8] A.M. Abakumov, J. Hadermann, S. Bals, I.V. Nikolaev, E. Antipov, G. Van Tendeloo, Angew. Chem. Int. Ed. 45 (2006) 6697.
[9] J. Hadermann, A. Abakumov, I.V. Nikolaev, E.V. Antipov, G. Van Tendeloo, Solid State Sci. 10 (4) (2008) 382.
[10] C. Lepoittevin, J. Hadermann, S. Malo, O. Perez, G. Van Tendeloo, M. Hervieu, Inorg. Chem. 48 (17) (2009) 8257.
[11] S. Malo, C. Lepoittevin, O. Pérez, S. Hébert, G. Van Tendeloo, M. Hervieu, Chem. Mater. 22 (2010) 1788.
[12] I.V. Nikolaev, H. D'Hondt, A.M. Abakumov, J. Hadermann, A.M. Balagurov, I.A. Bobrikov, D.V. Sheptyakov, V.Yu. Pomjakushin, K.V. Pokholok, D.S. Filimonov, G. Van Tendeloo, E.V. Antipov, Phys. Rev. B 78 (2) (2008) 024426.
[13] V. Raynova-Schwarten, W. Massa, D.Z. Babel, Z. Anorg. Allg. Chem. 623 (1997) 1048.
[14] L.G. Khvostantsev, L.F. Vereshchagin, A.P. Novikov, High Temp.–High Pressure 9 (1977) 637.
[15] C. Koch, Determination of core structure periodicity and point defect density along dislocations, Ph.D. Thesis, Arizona State University, 2002.
[16] H. D'Hondt, J. Hadermann, A.M. Abakumov, A.S. Kalyuzhnaya, M.G. Rozova, A.A. Tsirlin, R. Nath, H. Tan, J. Verbeeck, E.V. Antipov, G. Van Tendeloo, J. Solid State Chem. 182 (2) (2009) 356.
[17] M.A. Carpenter, C.J. Howard, Acta Crystallogr. B65 (2009) 134.
[18] M.W. Lufaso, P.M. Woodward, Acta Crystallogr. B60 (2004) 10.
[19] J. Rodriguez-Carvajal, M. Hennion, F. Moussa, A.H. Moudden, L. Pinsard, A. Revcolevschi, Phys. Rev B57 (1998) 5259.
[20] A. Okazaki, J. Phys. Soc. Jpn. 26 (1969) 870.
[21] A. Okazaki, J. Phys. Soc. Jpn. 27 (1969) 518.